Correspondence to:
Y. Liu,
ye.liu@smhi.se

The Assimilation of Temperature and Salinity Profile Observations for Forecasting the River–Estuary–Shelf Waters

Ye Liu[1] [ID], **Jiping Xie[2]**, **Zhiqiang Liu[3,4]** [ID], **Jianping Gan[4]** [ID], **and Jiang Zhu[5]** [ID]

[1]Swedish Meteorological and Hydrological Institute, Norrköping, Sweden, [2]Nansen Environmental and Remote Sensing Center, Bergen, Norway, [3]Department of Ocean Science and Engineering, Southern University of Science and Technology, Shenzhen, China, [4]Division of Environment and Sustainability & Department of Mathematics, Hong Kong University Of Science And Technology, Kowloon, Hong Kong, [5]Institute of Atmospheric Physics, Chinese Academy of Sciences, Beijing, China

Abstract Current down-scaling numerical modeling system around Hong Kong achieved a considerable prediction skill for the estuarine–shelf circulation off the Pearl River Estuary without data assimilation (DA). In order to further improve the reliability of this modeling system, the cost-effective Ensemble optimal interpolation approach is implemented to test the potential benefits from assimilating the cruise temperature and salinity (T/S) profiles to reproduce the variable coast waters. Regarding assimilation parameters (e.g., assimilation window, observation spatiotemporal scales, and ensemble composition), four parallel experiments are conducted in summer 2015. Against the assimilated T/S profiles, the vertical structures of the analyzed T/S are improved by the DA, although the waters experience strong mixing on the shelf. Compared with the run without DA, the root mean square errors of the predicted T/S are generally reduced by 9.8%–23.5% and 4.2%–14.0% in the assimilation runs. The results also show the salinity stratification is improved in the shelf by the assimilation of T/S profiles, although the improvement is sensitive to the selected ensemble and the assimilation window. Further, we investigate the impact of the temporal scales of the river-estuary-shelf (RES) waters on the assimilation results by the sampling of the model-state ensemble. The water exchanges between the estuary and the shelf are also better captured through this assimilation. The assimilation impact analysis shows that DA has advantages in reproducing the distribution of water masses of the RES waters, although the quality of the reproduced water mass distribution is related to the adopted sample ensemble in DA.

Plain Language Summary The river–estuary–shelf waters of the Pearl River Estuary have high spatiotemporal variability. In this research, we use a high-resolution model with data assimilation to obtain a reliable prediction of these waters. The temperature and salinity profiles are assimilated in the current system to test the potential benefits from the cruise profiles to reproduce the variable coast waters. Our experiments show that the prediction skill of temperature and salinity is improved by data assimilation. The water exchanges between the estuary and the shelf and the water mass distribution of the study regions are well captured through this assimilation.

1. Introduction

The circulation and hydrographic properties of the river–estuary–shelf (RES) waters off the Pearl River Estuary (PRE, Figure 1) are highly variable in space and time due to multi-forcing of tides, winds, and buoyancy from river discharge (Liu & Gan, 2020; Zu & Gan, 2015). These RES waters are shallower than 50 m with complex bathymetry and are driven by strong wind and tidal forcing as well as remote forcing from the neighboring basin circulation in the northern South China Sea (NSCS, Figure 1). The PRE bathymetry is characterized by a wide shallow western bank and two relatively deep navigation channels in the eastern segment. Hong Kong Waters are characterized as a coastal embayment that is influenced by the waters from the PRE to the west, from Mirs Bay to the east, and from the continental shelf off Hong Kong to the south. The annually averaged river discharge from the Pearl River to the continental shelf is ~10,000 m³ s⁻¹ (Zu & Gan, 2015). These buoyant waters rush out of the estuary and form a notable buoyant plume over the shelf. As a result, the interaction between the plume and the wind-driven shelf circulation changes the pattern
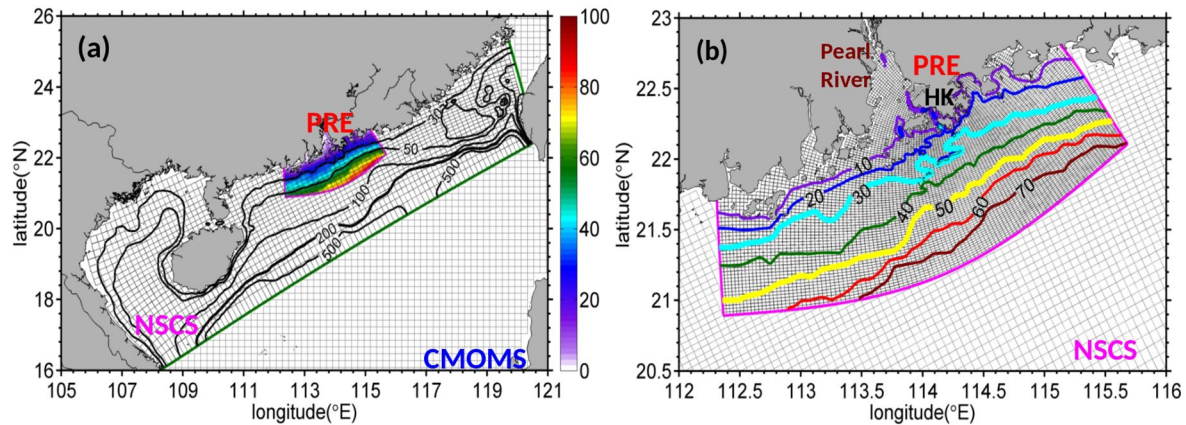
Figure 1. (a) The model domain, bathymetry (unit: m) and the isobaths (color lines) in the Pearl River Estuary and (b) the northern South China Sea (Liu & Gan, 2020) of the China Sea Multi-Scale Ocean Modeling System.

and intensity of the coastal circulation (Gan, Li, et al., 2009), which modulates the intrusion of the shelf water into the PRE. The river plume of the PRE shows complex and diverse structures under the influence of wind and tide. The enhanced mixing by tide retards the horizontal spreading process and increases the plume thickness, while the plume-induced stratification modifies the tidal current in turn. The PRE circulation interacting with the shelf circulation shows a distinct seasonal variation caused by the monsoon. Correspondingly, there is upwelling/downwelling of coastal waters in summer/winter along the PRE coast (Gan, Cheung, et al., 2009; Ji et al., 2011; Sheng et al., 2010), which increases the complexity of successfully forecasting the RES waters around Hong Kong.

The circulation around the PRE in response to tides, winds, and buoyancy discharge has been intensively investigated by various numerical studies (Gan et al., 2016; Gan, Li, et al., 2009; Ji et al., 2011; Lai et al., 2021; Luo et al., 2012; Ou et al., 2007; Zu & Gan, 2009, 2015). However, simulating the PRE waters has large uncertainties mainly due to complex hydrodynamics induced by the highly variable multi-forcing factors of winds, river discharge, and tides over the RES system. The challenges in the previous studies come either from spatiotemporally limited observations or from deficiencies in model physics such as sub-grid-scale parameterization of subscale processes (Liu et al., 2013). Therefore, combining model and observations is expected to be potentially more accurate than either model or observations used alone (Gregg et al., 2009).

There are many examples of developing coastal data assimilation (DA) techniques based on the Variational or Kalman Filter method (Moore et al., 2011), which have been widely used in a coastal area such as the New York Bight (Zhang et al., 2010), the Mediterranean (Korres et al., 2007; Teruzzi et al., 2018), the North/Baltic Sea (Liu et al., 2013, 2017), the California coast (Axell & Liu, 2016; Broquet et al., 2009; Li et al., 2015; Moore et al., 2011), the Gulf of Mexico (Counillon & Bertino, 2009), the Caribbean Sea (Powell et al., 2008), and NSCS (Shu et al., 2009; Xie et al., 2011). As a popular assimilation method, the ensemble optimal interpolation (EnOI) approach has been well applied in ocean researches, which uses a stationary ensemble composed of model states as a square root representation of the covariance matrix and it also does not require solving the adjoint equations of the dynamical system (Oke et al., 2008). As a consequence, this method is computationally cheap and is still 3-dimensional and multivariate. Furthermore, the effects of friction in RES models tend to damp down this mesoscale chaotic behavior. Fine-scale features such as eddy shedding in the chaotic behavior of upwelling and river plume filaments may be present. The water state in the RES system is more sensitive to vibrant dynamics due to the highly variable forcing of tide, wind, and buoyant discharge. As a result, the DA adjustment of the model simulation can be quickly dissipated by the swift changing wind- and tide-driven currents. Therefore, it is a challenge to capture the prediction uncertainty and extract reasonable observation information for a DA application in the RES dynamics waters. With sparse profile observations that may poorly resolve high-frequencies and spatial variations of these currents, the developed 'convention' DA scheme in the RES system (Figure 1) is a testbed for how to accommodate the dynamic characteristics with the improved DA skill and further benefits to other similar forecast systems.

This study objectively examines the DA system for the estuary–shelf model off Hong Kong to forecast the highly variable coastal waters. Based on the robust implementation of ensemble DA using the EnOI algorithm (Evensen, 2003) for forecasting the dynamics of coastal waters, we assess the DA performance (against observations) based on key metrics such as the water exchange and the distribution and variability of both temperature and salinity (T/S) in the RES waters. We characterize the abilities of the prediction system, with and without DA, to reproduce the observed water mass distribution as inferred from the sampled stations. This includes an evaluation of the influences of using DA in data-sparse dynamic coastal waters.

2. Ocean Model and Assimilation Method

2.1. The Coupled Estuary-Shelf Circulation Model

The Regional Ocean Modeling System (ROMS) (Shchepetkin & McWilliams, 2005) is used to simulate the estuarine and shelf circulations in the China Sea Multi-Scale Ocean Modeling System (CMOMS) which is composed of three simulations (Figure 1a). The large-scale circulations in the Northwestern Pacific Ocean and the South China Sea are simulated with a horizontal resolution of ~10 km (Gan et al., 2016). The horizontal resolution in the NSCS is downscaled to a finer resolution (~3 km) and then further downscaled to the model domain neighboring the PRE (Figure 1b). The active open boundary condition by Liu and Gan (2016, 2020) is used to interlink these simulations. Curvilinear orthogonal grids are used to implement a higher horizontal resolution (200–300 m) in the estuary and coastal regions. The grid size is gradually increased to ~1 km over the shelf at the southern boundary of this PRE simulation. The bottom topography is obtained by combining water depth data from the Hong Kong Maritime Department and the digitized high-resolution navigation charts published by the China Maritime Safety Administration. The model has 30 terrain-following vertical levels (Song & Haidvogel, 1994) and adopts higher resolutions (<0.2 m) in both the surface and bottom boundary layers to better resolve the dynamics inside these boundary layers.

The model is driven by the atmospheric forcing from the fifth generation of ECMWF atmospheric reanalysis (ERA5; Copernicus Climate Change Service (C3S), 2017). A time-dependent river discharge from the upstream hydrographic monitoring station at Gaoyao that is operated by the Ministry of Water Resources of China provides the buoyancy forcing from the estuaries. The impact from this variable river discharge is used to force the currents but ignored in the simulations to shed light on the roles of wind and tides on the plumes. Eight major tide components (M2, K1, S2, O1, N2, P1, K2, and Q1), which are extracted from the tidal assimilation model (Zu et al., 2008), have been used to implement the tidal forcing. The level-2.5 turbulent closure scheme from Mellor and Yamada's (1982) is used to parameterize the vertical mixing. A detailed description of model implementation and validation is described in Liu and Gan (2020).

2.2. Ensemble Optimal Interpolation (EnOI)

The EnOI algorithm has been applied previously in reanalysis applications and short-time forecasts of both open sea and coastal regions (Counillon & Bertino, 2009; Liu et al., 2014, 2017; Oke et al., 2008). EnOI computes an "optimal" oceanic state at a given time using observations, the predicted model state, and assumptions on their respectively unbiased error distributions. The relationship between them can be expressed as follows:

$$x^a = x^f + K\left(y - Hx^f\right), \tag{1}$$

$$K = P^f H^{\mathrm{T}}\left[H P^f H^{\mathrm{T}} + (N-1)R\right]^{-1}, \tag{2}$$

$$P = \frac{\alpha}{N-1} A'\left(A'\right)^T. \tag{3}$$

Here x is the model state vector which includes temperature, salinity, and current velocity. The superscripts a and f refer to "analysis" and "forecast", respectively. y is the observation vector. K is the so-called Kalman gain that weights the observational information based on the model and observation error covariance matrices, P and R, respectively. H is the observation operator that maps the model state onto the observation space, which searches the model grid closest to the observation position in this study. The subscript T denotes the transpose of a matrix. $A' = A - \bar{A}$ is an ensemble perturbation matrix. Here A and $\bar{A}$ are the

ensembles of model state vectors and the ensemble mean, respectively. N is the number of the ensemble samples, and the scaling factor $\alpha \in (0,1]$ is introduced to tune the covariance of the ensemble perturbations to capture the variability of model parameters. After a sensitivity analysis like Liu et al. (2013), the factor α with a value of 0.3 is used in all assimilation experiments. The ensemble of the model state vector is critical to the performance of an EnOI system. The scales of variability and features represented by the ensemble perturbations should resemble the dominant errors of the model (Oke et al., 2008). To evaluate the influence of the model errors at different scales on the EnOI analysis in the PRE simulations, two ensembles of model state vectors are used in this study. The samples were taken from the hindcast simulations without DA in both July 2014 and July 2015. The first ensemble uses daily mean fields of the model state and another ensemble uses the model snapshots at the time of 12:00 and 24:00, respectively. Hence, a total of 60 and 120 model samples are adopted for those two ensembles, respectively. The daily samples can catch the model variability higher than 24 hr, but the snapshot samples probably hold the information of model variability on a temporal scale shorter than 24 hr. Other "sophisticated" sample ensembles are of interested to be tested, but this is beyond the scope of this study.

As one of the most important designs in a DA system, the used observation errors directly affect the final assimilation results. For simplification, observation errors are assumed to be uncorrelated in this study. Thus, observation error covariance, R, is a diagonal matrix in which the diagonal elements are the observation error variances depended on the assimilated observation types and locations. Usually, when assimilating the profile of T/S, the observation errors are decreased from the surface to under the thermocline as proposed by Stammer et al. (2002) and used in Xie and Zhu (2010). Unresolved scales or processes in the RES observation are more complex relative to those in the open sea, which makes the representative error larger. Thus, compared to Xie and Zhu (2010), we adopted a larger observation error of T/S and calculated the standard deviations of observation errors of T/S as following equations,

$$\sigma_{\text{temp}} = 0.05 + 0.45 \times \exp\left(\frac{-d}{500}\right), \tag{4}$$

$$\sigma_{\text{salt}} = 0.3 + 0.2 \times \exp\left(\frac{-d}{125}\right), \tag{5}$$

where d represents the water depth (unit: m) at the observation position.

Localization is a crucial factor for EnOI to reduce the sampling error that arises from the use of small ensembles (Liu et al., 2013). With a quasi-Gaussian function given by Formula 4.10 in Gaspari and Cohn (1999), we only localized the model error covariance in the horizontal direction. Based on the statistic analysis of the sample ensembles (Figure 3), we adopted a uniform correlation scale of 20 km (Lai et al., 2021). Furthermore, we have selected a window of 24-hr in all assimilation experiments. All the observations collected within 24 hr are used to yield the "new" initial condition for the following assimilation cycle and these observations are assumed to be measured simultaneously. When observations become available at a certain time, the optimal state variables are calculated by the EnOI Equations, which are used as the new initial conditions of the next simulation cycle.

3. Observations and Experiments Designed

3.1. Observations in July 2015

The in situ data used in this study were extracted from the deployed Conductivity-Temperature-Pressure (CTD) profiler during a cruise conducted in July 2015. The temporal and spatial distribution of observations is shown in Figure 2. These observations were mainly located in the RES waters around Hong Kong. The cruise started on July 5th in the PRE and then sailed over the shelf from west to east. The cruise also reached Mirs Bay and ended in Hong Kong on July 30th. We established 152 stations in the estuary, Hong Kong Waters, and over the shelf. The horizontal distribution of these stations is shown in Figure 2a. Those sampling stations are over the 50-m to 10-m isobaths with a 5-m interval to better reveal the cross-shore exchanges of waters in the RES system. The maximum depths of CTD profiles are almost identical to the maximum water depths at the observational positions (Figure 2b). A CTD profiler was deployed to retrieve the hydrographic
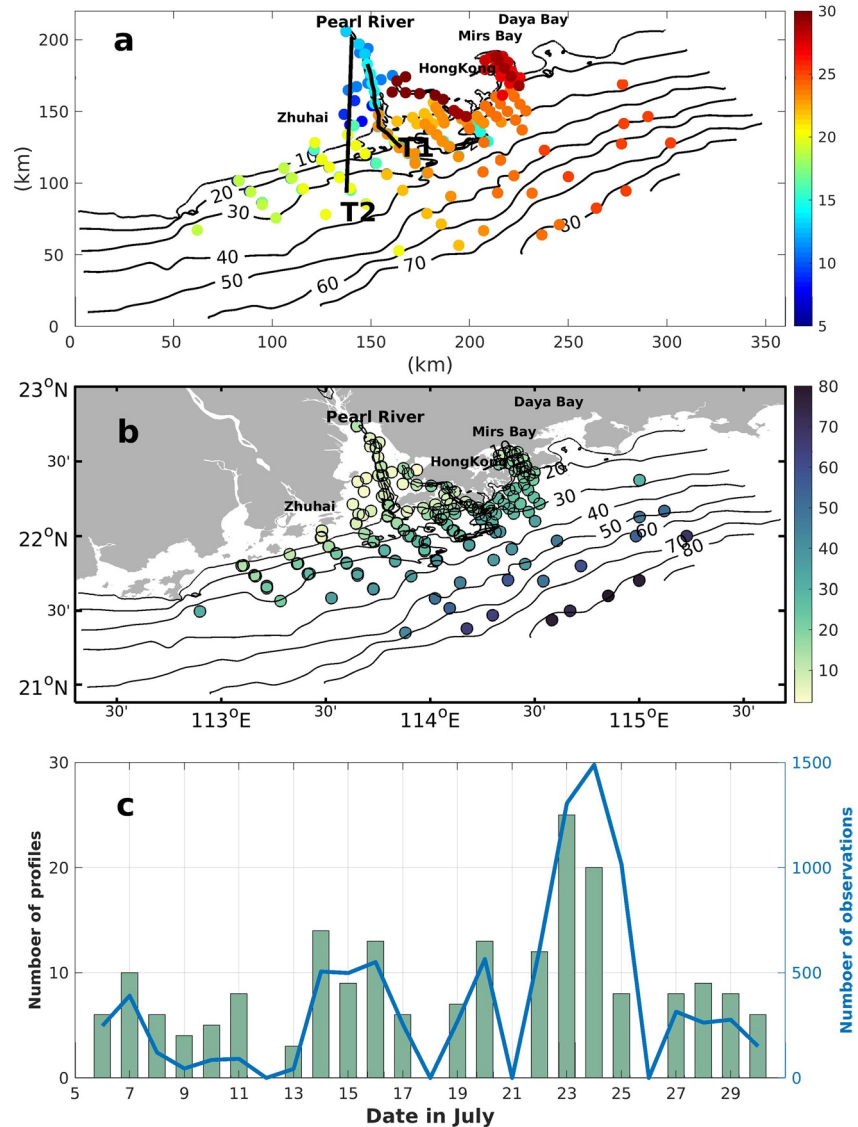
Figure 2. (a) Station locations are color-coded by the date of their occupation and the model domain in Cartesian coordinates. Black lines indicate sections T1 and T2 used in the analysis of Section 4.4; (b) the horizontal coverage and max depth (colorbar) of the observed Conductivity-Temperature-Pressure profiles; (c) the daily number of profiles (bars) and observations (blue line) for temperature (salinity), respectively.

properties (T/S) of the water column over 12 transects over the shelf, except for four days (on July 12th, 18th, 22nd, and 24th) without observation due to adverse weather conditions (Figure 2c).

In order to reduce the number of the actually assimilated observations for every model layer, we identify all measurements of every profile within a model layer and compute the average value of all these measurements to produce one super-observation. Furthermore, we have also removed T/S measurements that differed from model results more than a given threshold of 7 °C/7 g/kg. During the experiment period, there were 200 profiles in total collected in the PRE domain with the maximum number of profiles (measurement records) of 25(1,500), for both T/S, on July 23rd (July 24th) as shown in Figure 2c.

3.2. Experimental Runs and Evaluation Metrics

Given important issues of an EnOI DA system (e.g., the ensemble construction and assimilation window), a set of simulation experiments were conducted to assess the impact of DA on the RES forecast (Table 1).

Table 1
The Setup of the Experiments in This Study, t_0 Represents the Moment of Assimilation Time

Experiment	Elements of ensemble	Ensemble size	Assimilated observation types	Time window of assimilated observations	Obs. time window for validation
DA01	Daily mean fields	60	T/S Profiles	(t_0-12h, t_0+12h)	(t_0, t_0+24h)
DA02	Daily mean fields	60	T/S profiles	(t_0-24h, t_0)	(t_0, t_0+24h)
DA03	Snapshots	120	T/S profiles	(t_0-24h, t_0)	(t_0, t_0+24h)
NoDA	-	-	No observation	-	(t_0, t_0+24h)

The four experiments cover the field survey period from July 6 to July 30, 2015. A control run without data assimilation (NoDA) is used to identify the model uncertainties and as a benchmark to compare with the assimilation experiments. In other runs, we assimilated the observations into ROMS at 0000 UTC (t_0), and then the model ran a 1-day simulation ($t_0 + 24$ h) to the next DA time and repeated this assimilation process. To evaluate the influences of the assimilation window on model forecasts and the effects of assimilating CTD data, we adopted two assimilation window schemes by shifting the assimilation time position in the assimilation window. Using the daily average sample ensemble, two experiments named DA01 and DA02 assimilate the CTD observations with a different assimilation window every day. At each assimilation time, DA01 digested the observations collected in the previous 12 hr (t_0-12h) and the following 12 hr (t_0+12h). DA02 used observations collected in the previous 24 hr (t_0-24h). Furthermore, to study the influence of the sample scheme on the forecast results, the last assimilation run named DA03 adopts the snapshot ensemble which is constituted of the instantaneous states of the model and uses the same assimilation window as in DA02. It also should be noticed that the ensemble members in both DA01 and DA02 are 60, but 120 for DA03.

The 24-hourly forecast from four runs was assessed with all observations of T/S from the cruise in 2015 July (Table 1). We analyzed how much the DA could affect the prediction skill of T/S. To assess the experiment results, the daily averaged bias, root mean square error (RMSE), and normalized RMSE were calculated by the following formula:

$$\text{bias} = \frac{1}{N}\sum_{i=1}^{N}\left(y_i - Hx_i\right), \tag{6}$$

$$\text{RMSE} = \sqrt{\frac{1}{N}\sum_{i=1}^{N}\left(y_i - Hx_i\right)^2}, \tag{7}$$

$$\text{NRMSE} = \sqrt{\frac{1}{N}\frac{\sum_{i=1}^{N}\left(y_i - Hx_i\right)^2}{\sum_{i=1}^{N}\left(y_i - \overline{y}\right)^2}}, \tag{8}$$

where y_i and x_i are the ith observation and corresponding simulation fields. N is the number of observations during the evaluation period and H is the observation operator. The overbar indicates the average.

4. Results

4.1. Statistical Characteristics of the Ensemble and the Observations

Using the ensemble-based background error covariances, it is possible to derive the correlation structures from point measurement taken within the model domain. These spatial correlation structures give an indication of the influence region of observations for each location. An observation of surface temperature at the Pearl River results in a correlation structure (Figure 3a) that suggests this observation spreads information of the surface temperature to both, central and coastal regions surrounding this point. A surface observation at the mouth of the PRE (Figure 3b) yields information not only on the surrounding waters but also on many nearby shallow coastal locations. A surface observation at the shelf (Figures 3c and 3d) influences the surrounding waters in the up/downstream region. These typical spatial structures are contained in the background error covariance defined by the ensemble as Equation 3, and finally are used to spread the observational information to regions where no observations exist.
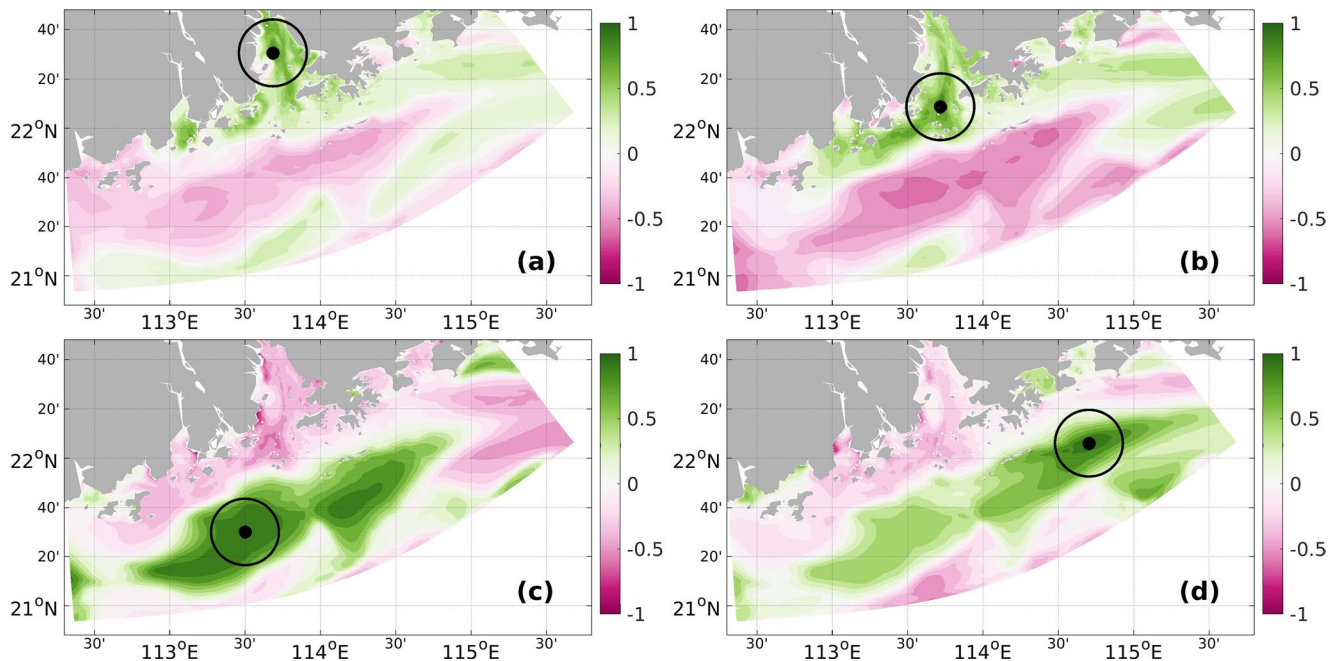
Figure 3. An example of the ensemble-based cross-correlation structure for a temperature observation in the surface cell for (a) Pearl River, (b) Pearl River Estuary, (c) shelf upstream region, and (d) shelf downstream region. Dark dots show the observation position and circles indicate the range of a 20-km influenced radius.

A temperature observation taken in the Pearl River has a footprint that positively correlates to most of the surrounding waters and negatively correlates to the shelf observations (Figures 3a and 3b). The opposite is the case for the observations from the shelf waters. The correlation structure depicted in Figures 3c and 3d suggests that an observation on the shelf has a relatively larger influence on the area along the currents than cross the currents. Further, an interesting phenomenon is the upstream shelf regions have a stronger correlation with the Pearl River waters than the downstream shelf regions (Figures 3c and 3d). These features make sense because this coastal system is affected by both the weather patterns and topography, which strongly influence the baroclinic dynamics (Trodahl & Lsachsen, 2018).

Comparing the sample ensemble to observations gives an indication of the distribution of the adjusted magnitude of DA from the EnOI equations. We calculated the error variances of the T/S from the snapshot ensemble in DA03 at the surface and bottom by Equation 3. As shown in Figure 4, the error variances of the ensemble are larger in surface water than those in bottom water. Regarding the surface temperature, the error variances at the western shelf waters are evidently larger than those around Hong Kong Island. The biggest error variance of surface temperature appears at western shelf waters, which is larger than 1.21 (°C)^2. However, the bottom temperature of the sample ensemble has different features. The bottom temperature of the sample has greater error variances in the western coastal waters and the Mirs Bay relative to that in other regions. Further, this ensemble has smaller error variances at the offshore shelf compared to that at other regions. Moreover, the sample temperature of the Pearl River has similar errors at both surface and bottom waters. Considering the surface salinity, the larger error variances occur at the western shelf and Pearl River compared to other regions. In general, the bottom salinity of the sample ensemble has smaller error variances relative to the surface salinity. However, the larger error variances of bottom salinity are still at the Pearl River. The feature shows salinity prediction is more challenging at the surface relative to at the bottom.

4.2. Quantitative Evaluation for Temperature and Salinity

To enable a quantitative validation of the impact of assimilating T/S profiles on the forecast, the forecast errors of the T/S from four experiments were calculated against in-situ observations. This calculation has
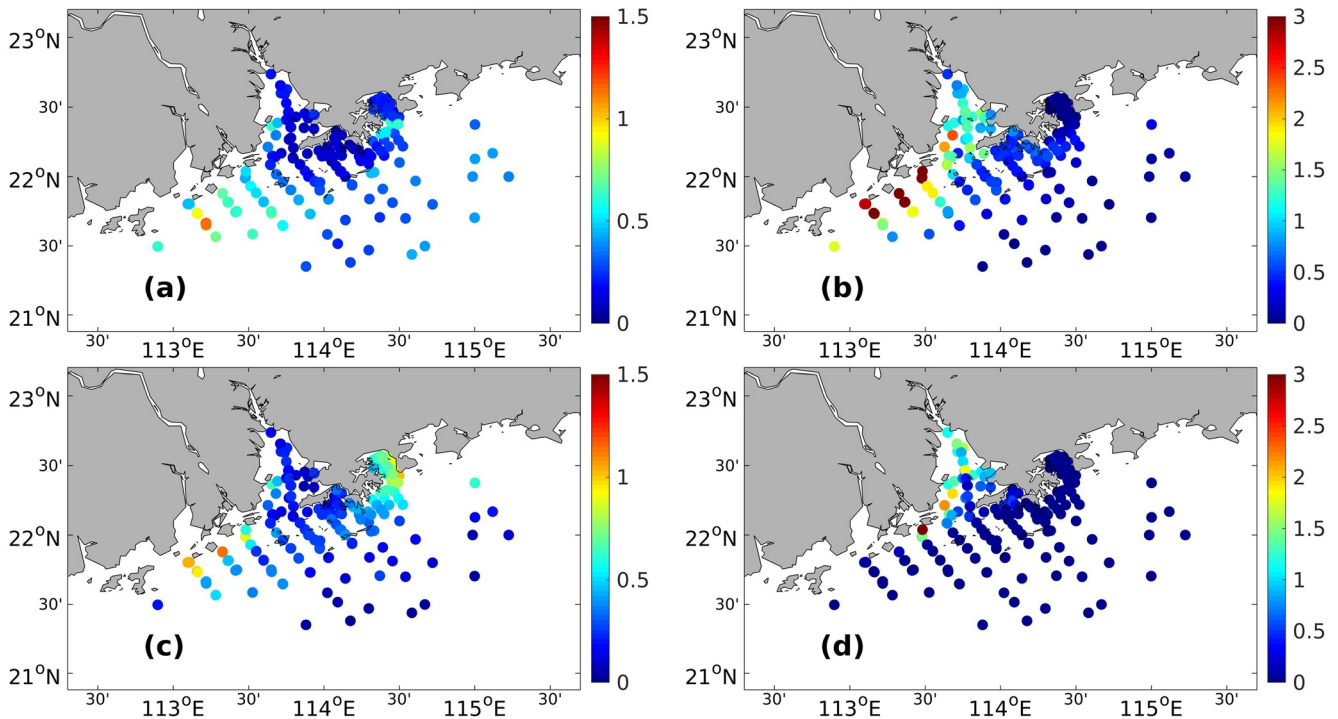
Figure 4. The error variances of the temperature (left panel; unit: (°C)^2) and salinity (right panel; unit: (g/kg)^2) from the snapshot ensemble in DA03 in the surface (a, b) and bottom (c, d) waters at the observation stations.

been performed prior to the assimilation and the errors are equivalent to forecast errors rather than analysis errors.

Figures 5a and 5b show the evolution of the T/S NRMSE simulated in experiments. This temperature NRMSE is generally decreased with the simulation evolution. As shown in Figure 5a, the NoDA has NRMSE beyond 1.0 during 8th–9th July and on 13th July. This indicates the model has an obvious deviation from the observations. However, the DA improved the model simulations for the stratification of T/S during these days (Figure 8). The maximum NRMSE for temperature in NoDA, 2.25, was decreased by 0.74–1.15 in the assimilation runs on July 9th. Although all assimilation experiments produced a better temperature relative to NoDA, their improvements have evidently different features. Overall, the NRMSEs for temperature were reduced by 13.9%–27.8% (from 0.72 for NoDA to 0.52–0.62 for the assimilation runs). The NRMSEs of temperature from the assimilation runs have similar variability over time. In terms of salinity, the overall NRMSEs of the assimilation runs were reduced by 4.6%–15.4% compared to that for NoDA (0.65). Therefore, the DA salinity has a smaller improvement than the DA temperature. In addition, the T/S improvements are not evenly distributed over time. On some days, the assimilation results are even worse than NoDA. The predictability improvements of the T/S in the DA runs are not always identical. As an example, DA improved temperature and degraded salinity on July 13th, respectively.

The overall NRMSE for T/S as a function of depth is shown in Figures 5c and 5d. The statistics are based on the comparison with all available profiles over the entire experiment period. First, the predicted values were interpolated to the observation positions with the observation operator and then the prediction mean bias was calculated by Equation 6. The comparisons in Figures 5c and 5d show that the temperature error in all the DA runs is smaller than that in NoDA. The NRMSEs of temperature were reduced at all depths. As a result, the overall RMSEs for temperature were reduced by 9.8%–23.5% (from 1.32 °C for NoDA to 1.01, 1.14, and 1.19 °C for DA01, DA02, and DA03, respectively). The better prediction of temperature in the DA runs is due to the reduction of both warm and cold biases (Figures 9 and 10). In waters shallower than 50 m, the global NRMSE of salinity decreases with increasing depth and the NRMSE of NoDA was reduced in the DA runs. However, in waters deeper than 50 m, the model has better performance than the DA runs. In general,
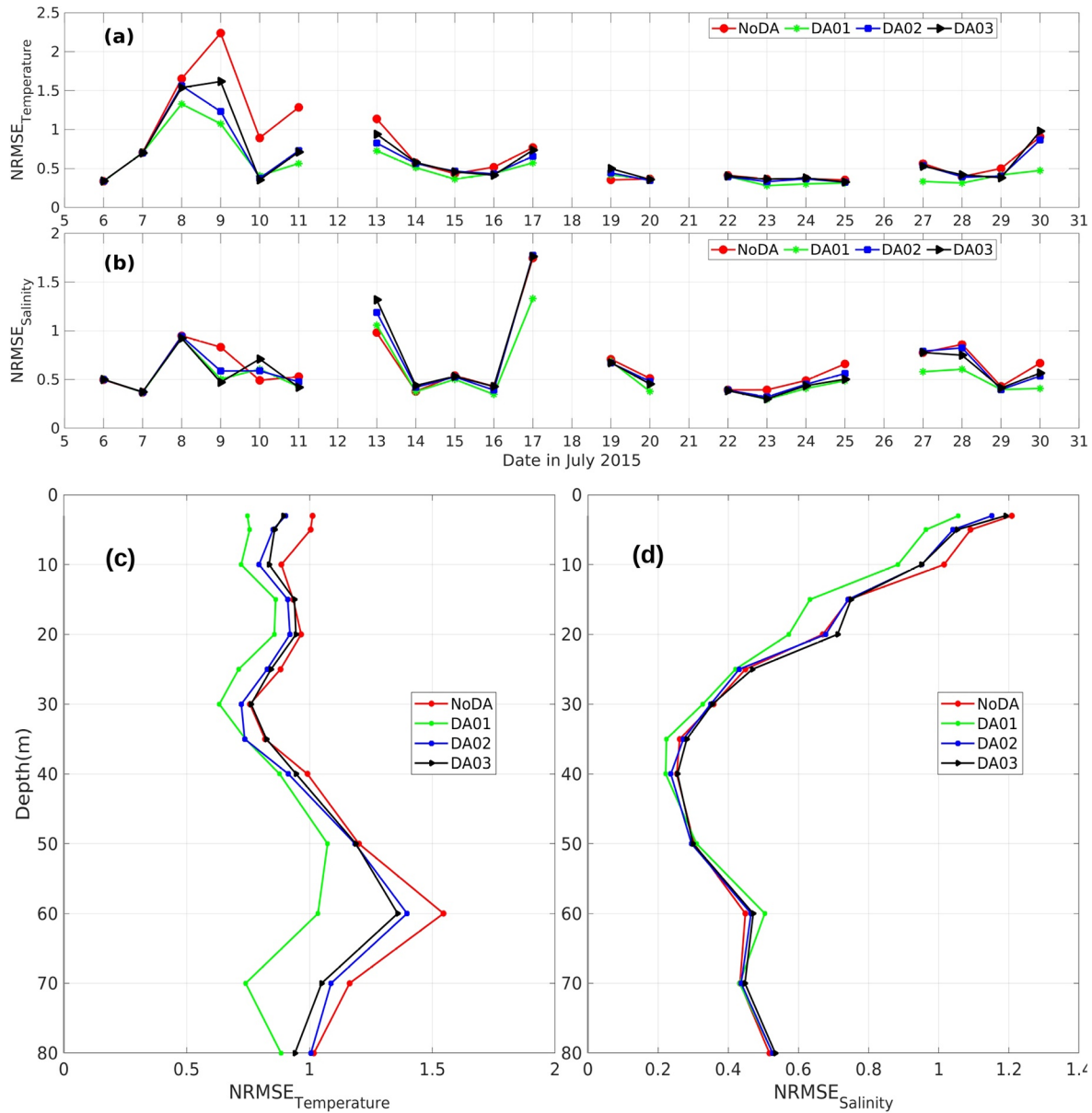
Figure 5. Daily mean NRMSE of temperature (a) and salinity (b) from forecast results relative to observations, and global NRMSE of temperature (c) and salinity (d) from forecast results against observations.

the salinity errors were reduced from 2.36 g/kg (NoDA) to 2.03 g/kg (DA01), 2.25 g/kg (DA02), and 2.26 g/kg (DA03), i.e., 4.2%–14.0% RMSEs have been reduced for salinity in the assimilation runs. Moreover, the NRMSE values exceeding 1.0 in Figure 5d indicate NoDA has low predictability for temperature in waters deeper than 40 m and salinity in waters less than 10 m deep, respectively.

4.3. Sensitivity Analysis of the Assimilation Configurations

The assimilation window can largely affect the analysis quality by controlling the available observations used for analysis. We assess the impact of the assimilation window on the PRE forecast. Two assimilation window schemes were designed for DA01 and DA02, respectively. The results show that DA01 has better performance for the T/S forecast compared to DA02 (see Figure 5). In general, the T/S RMSEs in DA01 were reduced by 11.4% and 9.8% relative to those in DA02 (Figure 6), respectively. Further, both errors of T/S are smaller in DA01 than those in DA02 at all depths and times. The reason is that the observation information
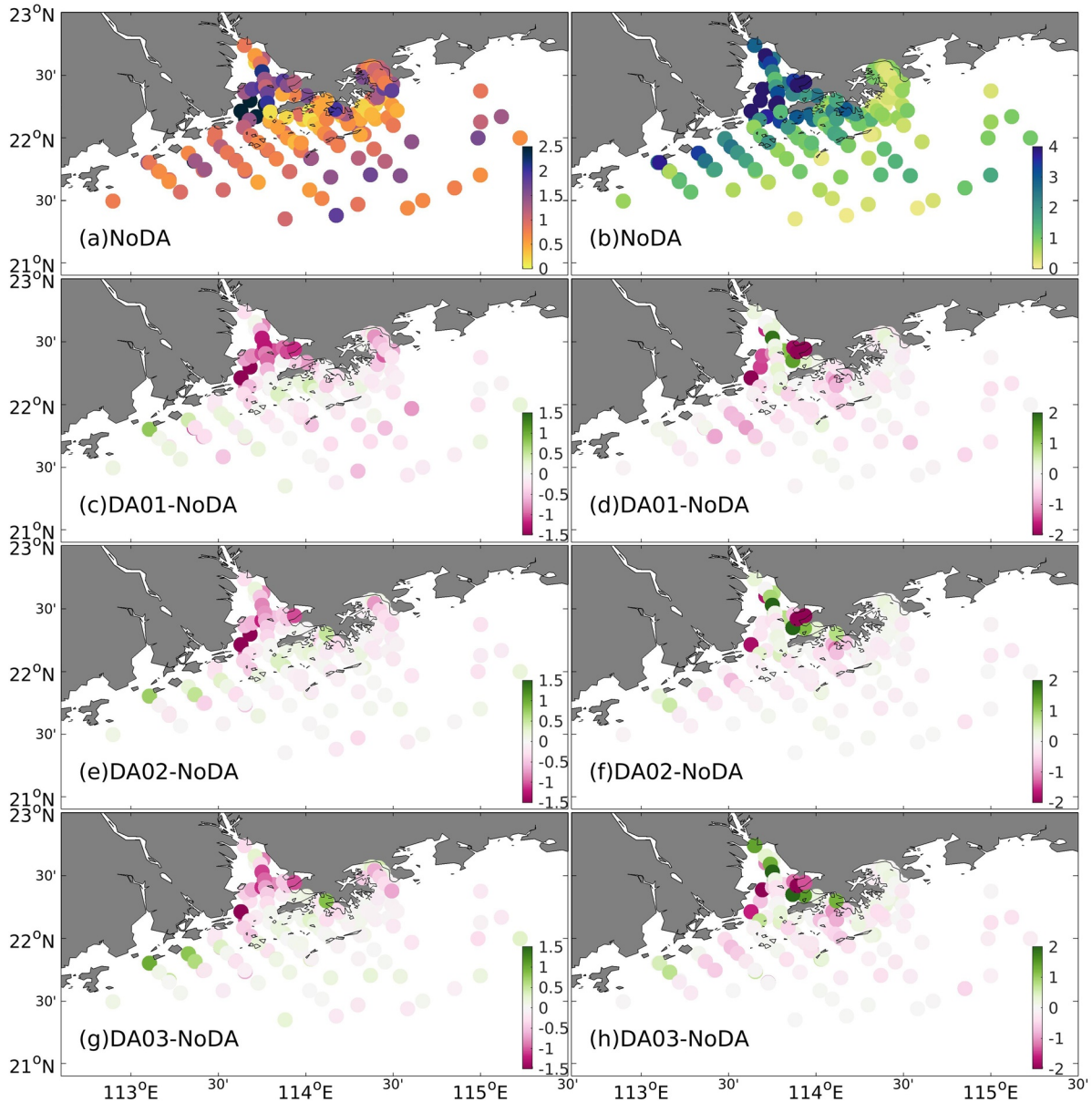
Figure 6. RMSE of temperature (left panel; unit: °C) and salinity (right panel; unit: g/kg) from NoDA relative to the CTD observations in July 2015 and the RMSE adjustments in DA01, DA02, and DA03 relative to NoDA.

entering the analysis processes for DA01 and DA02 is different although the length of the assimilation window is the same. First, the number of observations used for the analysis might be different because of the nonuniform distribution of observations over time. Second, to a first–half–day forecast of an assimilation cycle, DA01 could be constrained by the corresponding time-consistent observations and DA02 couldn't obtain any help from the time-consistent observations. In addition, the DA adjustment in a first–half–day influences the corresponding second–half–day forecast in the DA01 run. Third, to the same daily forecast, the second–half window for DA01 is closer to the assimilation time than the first–half window for DA02. Therefore, the observed values used in the second–half window of DA01 more accurately represent the true ocean state at the assimilation time relative to those in the first–half window of DA02. The comparison between DA01 and DA02 suggests that the choice of the observation time window for a DA system is very important to the prediction with DA of a region like the PRE where the T/S has large variability because of the strong tide and monsoon.

There are two schemes used here for choosing the sample ensemble based on different model error assumptions. To quantify the sensitivity of the forecast quality to the sample ensemble in the DA system, the RMSEs of T/S from the forecast against the observations are presented in Figure 6. The statistics presented are based on the comparisons with in-situ observations at all depths in July 2015. This comparison is used to show how much the model uncertainty in spatial scale is sensitive to the sampling scheme. The temperature from NoDA has maximum uncertainty in the Pearl River and minimum uncertainty in the Hong Kong Waters (Figure 6a). Over the shelf, larger and smaller errors of temperature are generally distributed in the downstream and upstream regions, respectively. To the salinity, the model has difficulty in reproducing good simulation for the PRE water. There are strong buoyancy exchanges between the PRE and the adjacent shelf waters. For example, although the model can well reproduce the shelf salinity and capture the main salinity feature of the PRE, it is hard to accurately simulate the salinity front caused by the outflowing low-salinity water from the PRE and the intruding salty water from the shelf (Figure 8). The comparisons in Figure 6 indicate that NoDA and the assimilation runs are comparable in most regions. In the PRE, DA significantly improved both T/S and the salinity variation seems more sensitive to the snapshot sample ensemble (also see Figure 9). For instance, the forecast errors in the PRE were reduced by 1.0 °C and 3.0 g/kg in the assimilation runs compared to those in NoDA. For the shelf water, DA03 degraded the temperature forecast at the southern boundary of the study region. The comparison between DA02 and DA03 shows the daily samples have advantages in decreasing the temperature errors in both the shelf and PRE waters and disadvantages in reducing the salinity errors in the waters around Hong Kong island relative to the snapshot samples (Figure 6).

4.4. The Assimilation Impact on the Prediction of Hong Kong Waters

In summer, buoyant waters from the PRE are mainly transported by a strong southwesterly monsoon. There is an exchange between the buoyant waters from the PRE and saltier waters from the shelf by the coastal current and tide. This exchange directly influences the shelf water properties (e.g., salinity and density). Thus, it is meaningful to verify the transport process of waters from the PRE and the ocean parameter's variation caused by DA. We present the volume transport simulated by NoDA at the surface and bottom as well as the vertically averaged transport in Figure 7. The volume difference transported in DA02 and NoDA is also shown in Figure 7. The NoDA results show that the coastal waters intruded into the PRE along the western coast of the PRE. The intruded water weakened and exited the estuary along the east coast of the estuary. Meanwhile, a notable upwelling jet, which is intensified in the lee of Hong Kong (Liu et al., 2018), is observed over the shelf. Water transport mainly happens on the shelf. The water transports are significantly larger in the downstream shelf and the surface than those in the upstream shelf and the bottom, respectively. Figure 7 shows water was gradually transported northward along the offshore from the west shelf to the east shelf. The transport variation caused by DA is mainly located on the western and southern shelf. Evidently, the decreased transport by DA at the entrance of the estuary weakened the saltwater intrusion and freshwater outflux. On the contrary, the increased transport is found further offshore over the shelf with the largest increment in the westernmost upstream Waters.

To further evaluate the variation of water exchange in the PRE, we compare the forecasted T/S along two cross-sections (T1 and T2, Figure 2) with the corresponding observations in Figures 8 and 9. The observations along T1 were collected from the PRE to the shelf including the PRE discharge region. Therefore, the observations are good to estimate the T/S variation in the PRE. At T1, it is observed that water flowed out of the PRE in the upper layer, which shows high temperature and low salinity. As a result, a salinity front and stratification were formed with the high salinity water from the shelf. NoDA well captured these characteristics. However, it overestimated the salinity of the PRE waters. This resulted in a weak salinity front and weak salinity stratification compared to the observations. Figure 8 shows that DA has improved the salinity simulation for the PRE. For example, in the shelf waters deeper than 10 m, the largest salinity reduction by DA reaches 4 g/kg. Consequently, the salinities from the assimilation experiments are almost consistent with the observation. In the PRE, the salinity in the near-surface water was overestimated in the assimilation forecasts. The increased salinity by DA in the upper/deepwater enlarged the discrepancy between the upper waters and the deep waters. Compared to the DA runs with both observations and NoDA, it could be concluded that DA increased and improved the salinity stratification intensity (Lai et al., 2021). DA also decreased the mixing of the water columns. This was also verified at T2 in Figure 9. The surface
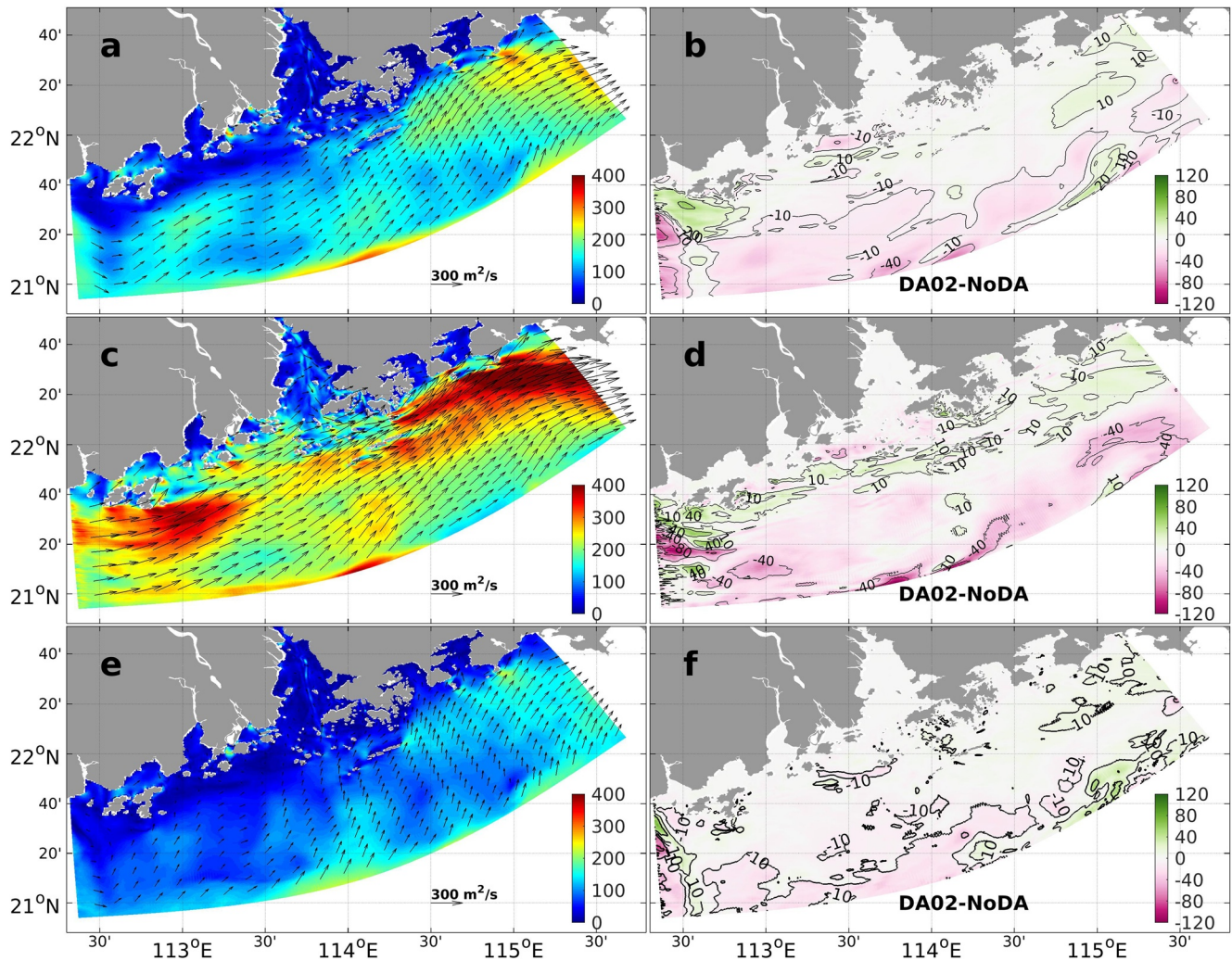
Figure 7. Modeled volume transport per unit depth (left panel; unit: m²/s) of the control run, the transport difference (right panel; unit: m²/s) between the DA02 and NoDA for vertical average (a and b), the surface (c and d) and bottom (e and f) at July 25, 2015, respectively. The arrows in the left panel show the direction and magnitude of transport.

and subsurface salinities outside the estuary were decreased in the DA runs relative to that from NoDA, whilst the salinities were increased in the Pearl River. The maximum reduction and increment of salinities appeared respectively in DA01 and DA03, and both of them reached 1.5 g/kg (Figure 9). The salinity reduction outside of the estuary and the salinity increment in the Pearl River enhanced the salinity front and hindered the water exchange. Figure 9 also shows the thermocline was enhanced by decreasing the bottom temperature in the shelf, which also proved that DA decreased the mixing of the water columns in the shelf. Furthermore, the comparison of the DA runs shows that DA01 has slightly better performance relative to other runs. For instance, in the PRE, the bottom salinity from DA01 is closer to observations than that in the other runs. Furthermore, compared to observations at the shelf surface, the salinities obtained in both DA01 and DA02 are better than the results from DA03 (Figure 8). In terms of temperature, the warm and cold biases in NoDA are found in the PRE and at the shelf surface, respectively. At the shelf bottom, DA eased the warm bias in both the PRE and the surface shelf waters, whilst there aren't any significant variations in the deep shelf waters.

At the west coast of the PRE, Figure 9 shows the T/S with and without DA at section T2 on July 25. The NoDA simulation has well captured the salinity stratification and the saline water intrusion in this section. In addition, the temperature is colder at the western bank than at the eastern bank in the PRE. After DA,
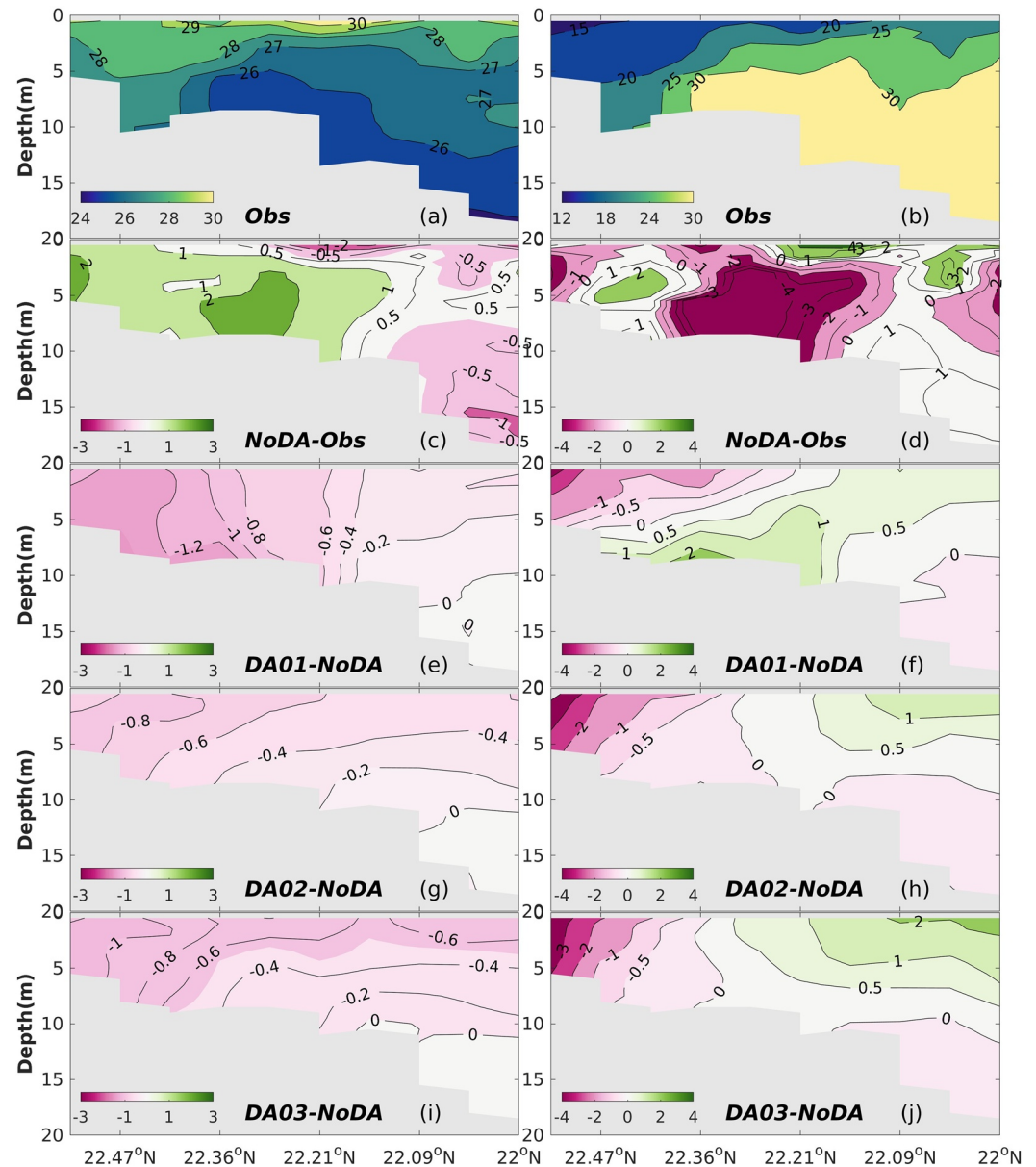
Figure 8. The temperature (left panel; unit: °C) and salinity (right panel; unit: g/kg) profiles observed along T1 (Figure 2a) on July 15, 2015; The prediction deviations of temperature and salinity in NoDA and the DA improvements of temperature and salinity relative to NoDA in DA01, DA02, and DA03, respectively.

the T/S at T2 has changed. For example, the temperature at T2 varied by DA mainly at the estuary and below the shelf thermocline, whereas waters from the PRE didn't show notable changes in temperature. For the salinity at T2, large changes appear in the mixed layer of the RES waters. In general, the T/S from DA03 has a smaller (larger) variation than that from DA02 (DA01), respectively, especially in the PRE. Furthermore, the DA03 yielded an increment similar to the DA01 and DA02.

Assimilating T/S can cause variations in the distribution of water masses. Figure 11 shows the T–S diagram of the observations and the experiment runs at all cruise stations. Here, we categorize the water masses into four types: the water mass from the PRE with salinity less than 30 g/kg and temperature larger than 28.1 °C; the surface shelf water mass with salinity greater than 30 g/kg and temperature larger than 25.1 °C; the subsurface shelf water mass with temperature less than 25.1 °C and salinity greater than 30 g/kg; and the mixed water mass between the PRE water and the surface shelf water with salinity smaller than 30 g/kg and
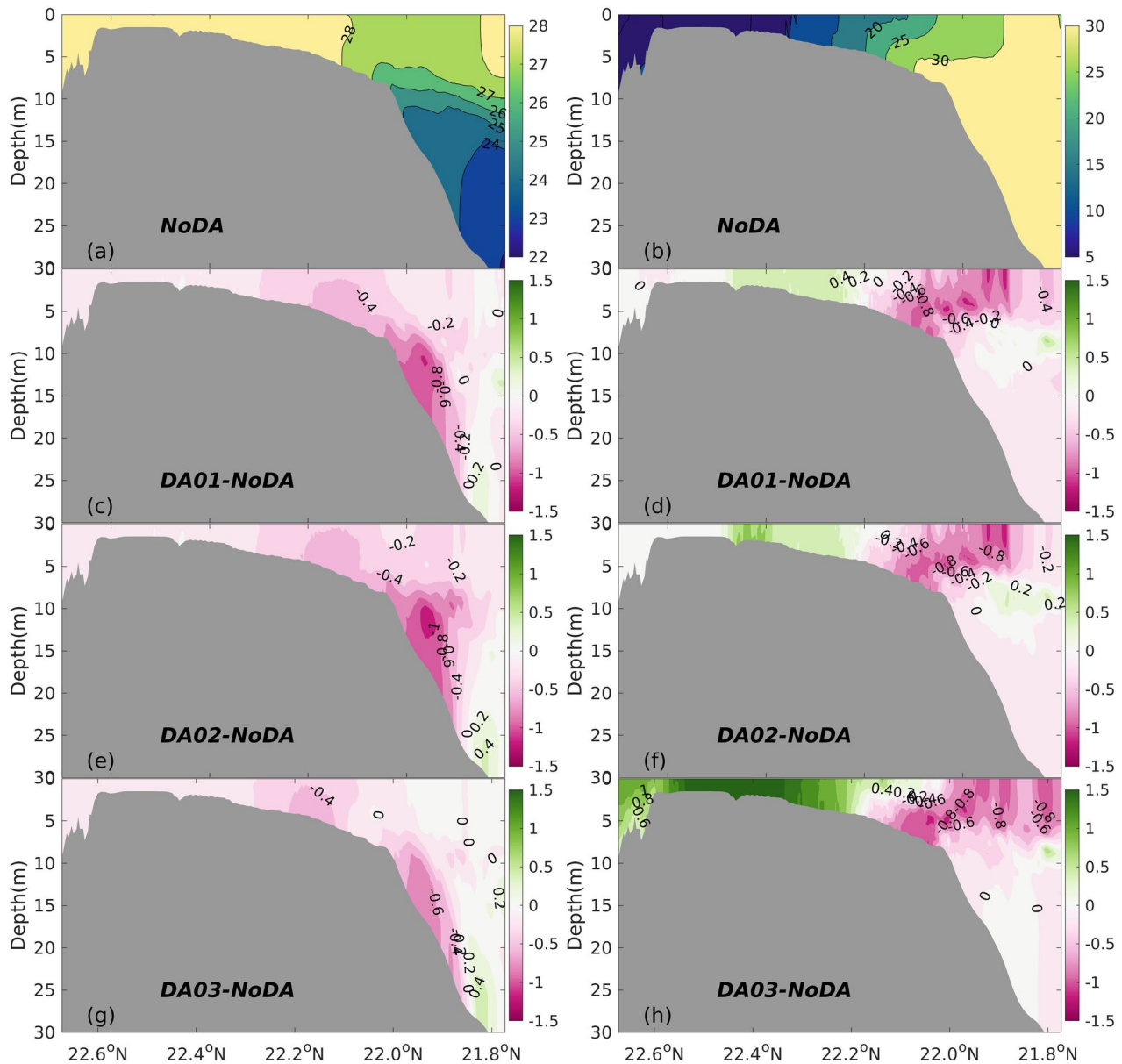
Figure 9. The cross-section (T2, Figure 2a) temperature (left panel; unit: °C) and salinity (right panel; unit: g/kg) simulated by the model, the simulation increment of the assimilation experiments on July 23, 2015.

temperature smaller than 28.1 °C. As illustrated in Figure 11, all experiments reproduced these four water masses with different accuracy. However, compared to the observed one, NoDA shows the shelf water mass is colder at the surface and fresher at the subsurface, respectively. Furthermore, to the Pearl River water, NoDA is saltier and warmer relative to the observed one. For example, NoDA produced much water with a temperature between 28.1 and 31.0 °C and salinity less than 13 g/kg. However, these waters haven't been observed. The Pearl River water in the assimilation runs agreed with the observations much better. The assimilation runs are also verified in the subsurface water, the water warmer than 35.0 °C is observed, which is not shown in NoDA but is shown in the DA runs. Apparently, the DA experiments generally produced a better distribution of the water mass in the RES waters off the PRE. The eastward transport at the estuary was weakened by DA. Therefore, less freshwater can flow out of the PRE in the DA runs and more freshwater in the PRE is simulated. DA also strengthened the intrusion of saline water from the shelf. As a result, the water of the mixed water mass was increased in the deeper layers. Below the thermocline, over the shelf,
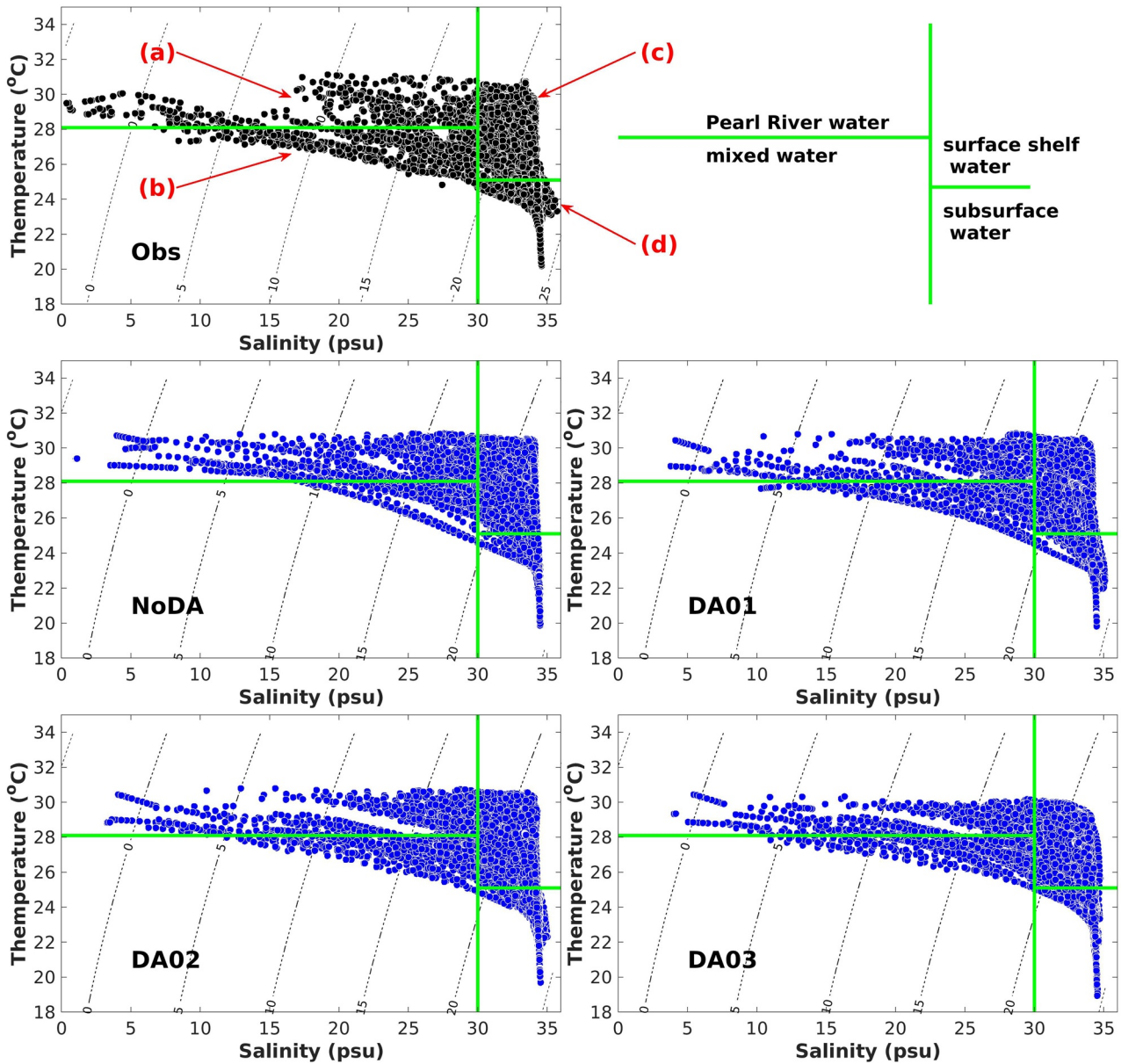
Figure 10. T–S diagram of all sampling stations for observation, NoDA, and data assimilation experiments, respectively. The contour lines denote the sigma-t density (unit: kg/m³). The arrows show where data assimilation has improved.

the improvement of water mass is also visible in the assimilation runs, where the salinity in NoDA is fresher than the observed salinity. Further, compared to NoDA, DA03 changed the freshwater in the PRE too much and worsened the distribution of the freshwater, whereas DA01 (DA02) has not significantly degraded the simulation of the PRE water. Moreover, the water mass below the shelf thermocline in both DA01 and DA02 is slightly closer to the observed one compared to that in DA03.

5. Discussion

Our assessment is influenced by the spatial and temporal distribution of the validating observations. Liu et al. (2009) used a single observation to show how the adjustment by an upstream observation influences the downstream region in the shallow and narrow Straits. In this study, We assessed the general influences of all observations and presented the impact of the observation distribution on the DA results in the PRE.
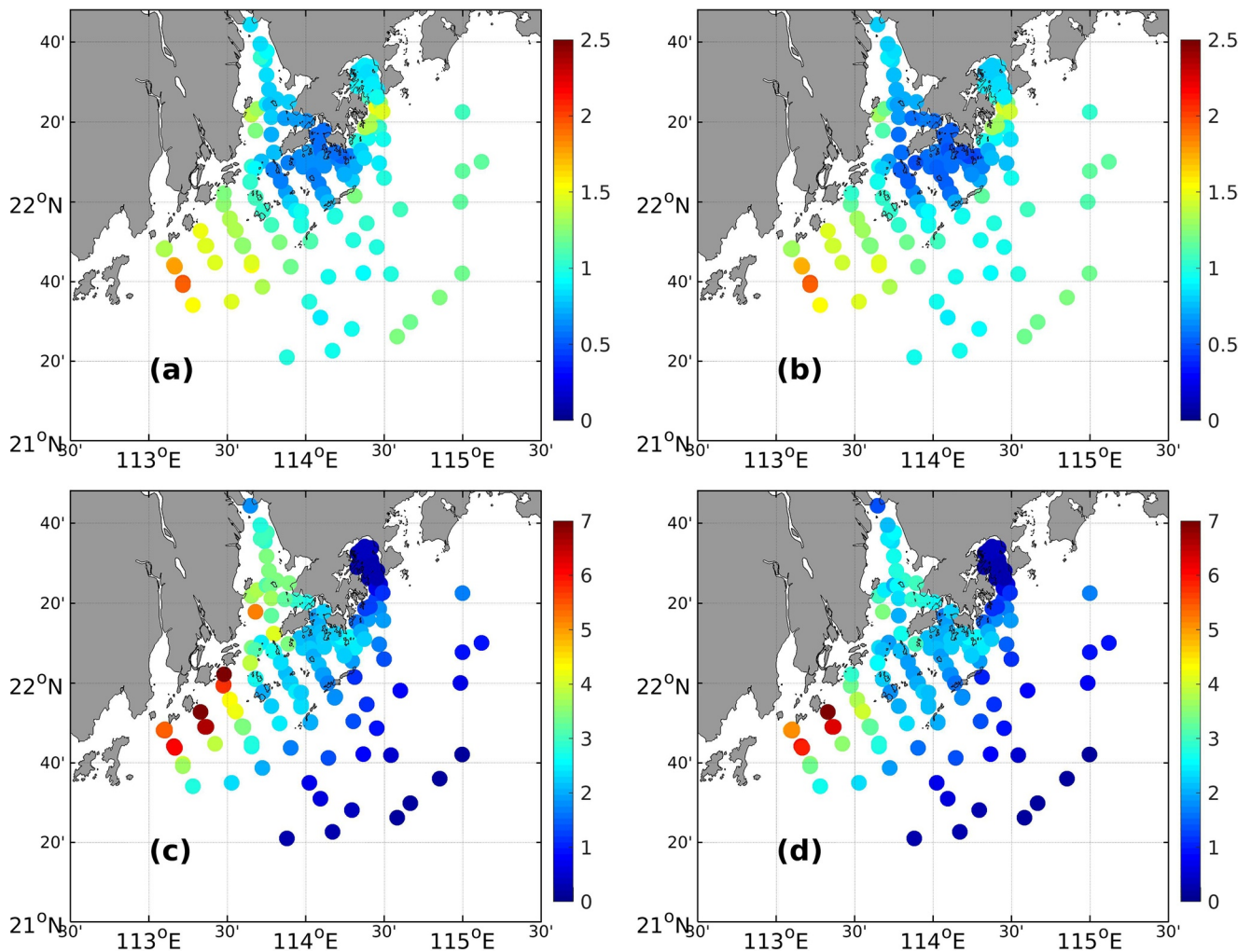
Figure 11. The standard deviation of temperature (a and b; unit: °C) and salinity (c and d; unit: g/kg) from ensemble samples with (a and c) and without (b and d) tidal signal on the mean surface layer (0–5 m) at the Conductivity-Temperature-Pressure profiles.

The cruise moved generally eastward over the month of July 2015. The PRE circulations and tides are influenced by the summer monsoon and the DA adjustments of T/S in the earlier observed areas could be transported to the downstream regions by currents and tides. So the earlier observations may have an impact on the newly observed area. This may be especially true as the cruise moves into different regimes (river month, outer shelf, bays, etc.). The evaluation in Figure 5 denotes that the improvement of T/S is greater in the mid-to-late period than in the early period of July 2015. Another example for this is that the modeled fields have a larger error in the western shelf (upstream region) than that in the eastern shelf (downstream region) (see Figure 6).

An appropriate assimilation window could benefit DA results by increasing observation information, especially for the region where it is difficult to collect observations. However, when an assimilation cycle is carried out in a coastal region like the PRE, too large an assimilation window may bring unreasonable observations into an analysis process, and this may cause failure analysis. On the contrary, if an assimilation window is too short, important observation information may be lost and result in a worse analysis constraint (Liu et al., 2009). Lai et al. (2021) showed the influences of observations on the PRE forecast by using different assimilation window lengths and selecting the observations in the same assimilation window. In contrast to Lai et al. (2021), at every assimilation cycle of this study, we used an assimilation window with the same length but different assimilation time setup to emphasize the importance of the assimilation window for the PRE prediction. Both Lai et al. (2021) and this study indicate that choosing observations

at a different time has distinct DA performance of the PRE forecast. The observations may imply dynamic features of the RES region off Hong Kong (Lai et al., 2021). For example, the observed salinity discrepancy of the PRE reaches 7 g/kg in a different stage of a flood–ebb period. A more robust time window would be interesting to be studied for successful assimilation for a dynamic estuary–shelf system. For example, the selection of the DA time window associated with regional physics and the number of observation samples considering spatial variability in a simulated region like the PRE.

We used different numbers of samples in DA01(DA02) and DA03, the ensemble size may be another factor to influence the DA results of this study. To examine this, we stored snapshots in July 2014 and July 2015 every 2 hr as a sample pool. From this sample pool, we randomly generated three snapshots ensembles with different sizes (60, 110, and 336) and three other daily averaged field ensembles with sizes of 35, 40, and 50. Then we compared the standard deviations (SDs) of these ensembles and the results didn't show an evident variation in the T/S SDs of the snapshot ensembles and the daily averaged ensembles, respectively. According to the EnOI equations, the ratio of |P| and |R| defines the "strength of attraction" of the forecast to the observations, which determines the DA adjustment. We used a stationary observation error covariance in all assimilation experiments. Therefore, the DA result of an EnOI system is directly controlled by |P|. To our sample pool, the SDs of those new ensembles indicate that the ensemble size isn't a key influence factor to the DA results in this study. The tidal signals in an ensemble may cause a large DA adjustment of salinity in both the mixed layers and the thermocline. To a snapshot ensemble, the surface fields retain the strong tidal signals (Figure 7), which are good to exhibit the effect of the tidal signals on DA. The tidal current with diurnal periods are dominant in the PRE waters (Lai et al., 2021). We used a 24-hour window to filter out the tidal signals from snapshots. The tidal signal in the ensemble leads to a large SD of the surface T/S, especially for waters along the western coastline of the Pearl River (see Figure 11). Compared to DA02, the larger adjustments of T/S at T1/T2 in DA03 are likely caused by unfiltered tidal signals in the ensemble, whilst DA03 produced a better prediction than DA02 for the shelf salinity and the Pearl River temperature when compared to the observations (see Figures 8 and 9). Therefore, an ensemble with tidal signals performed better than an ensemble without tidal signals for the salinity in the shelf and for temperature in the Pearl River, respectively.

6. Summary and Conclusions

In this study, a DA system based on the EnOI method was applied for assimilating T/S profiles for the prediction of the RES waters off the PRE. A set of simulation experiments was used to evaluate the effectiveness of this DA system in an application to coastal waters encompassing a wide range of dynamic spatial scales. The DA system also allows the use of sparse profile observations. According to the dynamic features of the RES waters off the PRE, we examined the flexibility of the DA system implemented with the different sampling frequencies to address the T/S variability due to the multi-forcing of tides, winds, river runoff, and shelf currents. We also presented the importance of extracting reasonable observed information for the simulation of the RES waters off the PRE. Furthermore, the observation error was designed to vary with depth; this was done to model the complexity of unsolved processes and dynamics in the RES observations.

Based on the model–data comparison presented in this study, the simulation without DA shows evident biases in both T/S. The reasons for these biases are not totally understood yet, although it is inferred that the main reasons might be related to the imperfect initial conditions, biased forcing fields, and the limitations of model parameterizations. In general, DA has significantly increased the prediction skill of T/S, resulting in better simulations of T/S. During the experiment period, calculated with all observations, the overall RMSEs of T/S were reduced by 9.8%–23.5% and 4.2%–14.0% in the DA forecasting, respectively. Therefore, the sample ensembles and the observation error used in this DA system are suitable for improving the forecast of Hong Kong Waters.

The experiments were performed with different assimilation windows and sampling ensembles. We found that selecting a reasonable assimilation window is important to a DA simulation in a coastal region similar to the RES off the PRE, although we only assessed the assimilation window with the same length in the DA runs. Besides, the experiment results reveal that, to the water outside the PRE, the daily samples have advantages in reducing the warm bias and disadvantages in reducing the low salinity bias compared to the

snapshot samples (Figure 8). In the PRE, the salinity adjustment of DA is more sensitive to the snapshot samples than the daily mean samples (Figure 9). The DA with daily mean samples and the assimilated time in the center of the time window gives a better prediction of T/S than the other simulations in the PRE. It also should be noted that our conclusions are only based on all samples in July of 2014 and 2015.

The experiment results were also validated with daily T/S observations in Hong Kong Waters. According to the EnOI equations, the assimilation of the T/S profile places an integral constraint on the total water volume. However, the main variation by DA is manifested in the upper layers. Therefore, the results show that the low salinity biases at the bottom predictions were hardly changed by DA relative to the high salinity biases in the upper layers. Based on the T/S at the selected cross-sections, we found that both the salty water intrusion and the fresher water outflow were captured by NoDA. However, the water exchanges between the PRE and the shelf contained substantial biases in NoDA. The change in currents in the DA experiments has a relatively small magnitude at the bottom compared to that at the surface. Both the stratification and the salinity front in the PRE have been weakened in the assimilation runs and are closer to the observations compared to those in NoDA. This implies DA is able to reduce the exchange bias. Further analysis with passive tracers is necessary to show the impact of the DA on a longer time scale. DA is also helpful in improving the simulation of the water masses in the PRE (Figure 10). Below the thermocline over the shelf, the salinity from NoDA is smaller than the observed value, whereas the salinity in the DA runs is reasonably improved. Moreover, the daily mean sample ensemble has an advantage in the water mass simulation in both the PRE and the water below the shelf thermocline relative to the snapshot-sample ensemble, especially for the freshwater in the PRE.

Conflict of Interest

The authors declare no conflicts of interest relevant to this study.

Data Availability Statement

The datasets and model used for this research are included in Liu and Gan (2020).

References

Axell, L., & Liu, Y. (2016). Application of 3-D ensemble variational data assimilation to a Baltic Sea reanalysis 1989–2013. *Tellus A*, 24220. https://doi.org/10.3402/tellusa.v68.24220

Broquet, G., Edwards, C. A., Moore, A. M., Powell, B. S., Veneziani, M., & Doyle, J. D. (2009). Application of 4D-variational data assimilation to the California Current System. *Dynamics of Atmospheres and Oceans*, *48*, 69–92. https://doi.org/10.1016/j.dynatmoce.2009.03.001

Copernicus Climate Change Service (C3S). (2017). ERA5: Fifth generation of ECMWF atmospheric reanalyses of the global climate. In *Copernicus Climate Change Service Climate Data Store (CDS), date of access*. Retrieved from https://cds.climate.copernicus.eu/cdsapp#!/home

Counillon, F., & Bertino, L. (2009). Ensemble optimal interpolation: Multivariate properties in the Gulf of Mexico. *Tellus A*, *61*, 296–308. https://doi.org/10.1111/j.1600-0870.2008.00383.x

Evensen, G. (2003). The Ensemble Kalman Filter: Theoretical formulation and practical implementation. *Ocean Dynamics*, *53*, 343–367. https://doi.org/10.1007/s10236-003-0036-9

Gan, J., Cheung, A., Guo, X., & Li, L. (2009). Intensified upwelling over a widened shelf in the northeastern South China Sea. *Journal of Geophysical Research: Oceans*, *114*, C09019. https://doi.org/10.1029/2007JC004660

Gan, J., Li, L., Wang, D., & Guo, X. (2009). Interaction of river plume with coastal upwelling circulation in the northeastern South China Sea. *Continental Shelf Research*, *29*(4), 728–740. https://doi.org/10.1016/j.csr.2008.12.002

Gan, J., Liu, Z., & Liang, L. (2016). Numerical modeling of intrinsically and extrinsically forced seasonal circulation in the China Seas: A kinematic study. *Journal of Geophysical Research: Oceans*, *121*, 4697–4715. https://doi.org/10.1002/2016jc011800

Gaspari, G., & Cohn, S. E. (1999). Construction of correlation functions in two and three dimensions. *Quarterly Journal of the Royal Meteorological Society*, *125*, 723–757. https://doi.org/10.1002/qj.49712555417

Gregg, W. W., Friedrichs, M. A. M., Robinson, A. R., Rose, K. A., Schlitzer, R., Thompson, K. R., & Doney, S. C. (2009). Skill assessment in ocean biological data assimilation. *Journal of Marine Systems*, *76*, 16–33. https://doi.org/10.1016/j.jmarsys.2008.05.006

Ji, X., Sheng, J., Tang, L., Liu, D., & Yang, X. (2011). Process study of circulation in the Pearl River Estuary and adjacent coastal waters in the wet season using a triply nested circulation model. *Ocean Modelling*, *38*, 138–160. https://doi.org/10.1016/j.ocemod.2011.02.010

Korres, G., Hoteit, I., & Triantafyllou, G. (2007). Data assimilation into a Princeton Ocean Model of the Mediterranean Sea using advanced Kalman filters. *Journal of Marine Systems*, *65*, 84–104. https://doi.org/10.1016/j.jmarsys.2006.09.005

Lai, W., Gan, J., Liu, Y., Liu, Z., Xie, J., & Zhu, J. (2021). Assimilating in situ and remote sensing observations in a highly variable estuary-shelf model, *Journal of Atmospheric and Oceanic Technology*. https://doi.org/10.1175/JTECH-D-20-0084.1

Li, Z. J., McWilliams, J. C., Ide, K., & Farrara, J. D. (2015). Coastal ocean data assimilation using a multi-scale three-dimensional variational scheme. *Ocean Dynamics*, *65*, 1001–1015. https://doi.org/10.1007/s10236-015-0850-x

Liu, Y., Meier, H. E. M., & Axell, L. (2013). Reanalyzing temperature and salinity on decadal time scales using the ensemble optimal interpolation data assimilation method and a 3-D ocean circulation model of the Baltic Sea. *Journal of Geophysical Research: Oceans*, *118*, 5536–5554. https://doi.org/10.1002/jgrc.20384

Liu, Y., Meier, H. E. M., & Eilola, K. (2014). Improving the multiannual, high-resolution modelling of biogeochemical cycles in the Baltic Sea by using data assimilation. *Tellus A*, *66*, 24908. https://doi.org/10.3402/tellusa.v66.24908

Liu, Y., Meier, H. E. M., & Eilola, K. (2017). Nutrient transports in the Baltic Sea – Results from a 30-year physical–biogeochemical reanalysis. *Biogeosciences*, *14*, 2113–2131. https://doi.org/10.5194/bg-14-2113-2017

Liu, Y., Zhu, J., She, J., Zhuang, S. Y., Fu, W. W., & Gao, J. D. (2009). Assimilating temperature and salinity profile observations using an anisotropic recursive filter in a coastal ocean model. *Ocean Modelling*, *30*, 75–87. https://doi.org/10.1016/j.ocemod.2009.06.005

Liu, Z., & Gan, J. (2016). Open boundary conditions for tidally and subtidally forced circulation in a limited-area coastal model using the Regional Ocean Modeling System (ROMS). *Journal of Geophysical Research: Oceans*, *121*, 6184–6203. https://doi.org/10.1002/2016JC011975

Liu, Z., & Gan, J. (2020). A modeling study of estuarine–shelf circulation using a composite tidal and subtidal open boundary condition. *Ocean Modelling*, *147*, 101563. https://doi.org/10.1016/j.ocemod.2019.101563

Liu, Z., Gan, J., & Wu, X. (2018). Coupled summer circulation and dynamics between a bay and the adjacent shelf around Hong Kong: Observational and modeling studies. *Journal of Geophysical Research: Oceans*, *123*, 6463–6480. https://doi.org/10.1029/2018jc013830

Luo, L., Zhou, W., & Wang, D. (2012). Responses of the river plume to the external forcing in Pearl River Estuary. *Aquatic Ecosystem Health & Management*, *15*(1), 62–69.

Mellor, G. L., & Yamada, T. (1982). Development of a turbulence closure model for geophysical fluid problems. *Reviews of Geophysics and Space Physics*, *20*, 851–875. https://doi.org/10.1029/rg020i004p00851

Moore, A. M., Arango, H. G., Broquet, G., Edwards, C., Veneziani, M., Powell, B., et al. (2011). The Regional Ocean Modeling system (ROMS) 4-dimensional variational data assimilation systems. Part II: Performance and application to the California Current System. *Progress in Oceanography*, *91*, 50–73. https://doi.org/10.1016/j.pocean.2011.05.003

Oke, P. R., Brassington, G. B., Griffin, D. A., & Schiller, A. (2008). The Bluelink ocean data assimilation system(BODAS). *Ocean Modelling*, *21*, 46–70. https://doi.org/10.1016/j.ocemod.2007.11.002

Ou, S., Zhang, H., & Wang, D. (2007). Horizontal characteristics of buoyant plume off the Pearl River Estuary during summer. *Journal of Coastal Research*, *50*, 652–657.

Powell, B. S., Arango, H. G., Moore, A. M., Di Lorenzo, E., Milliff, R. F., & Foley, D. (2008). 4DVAR data assimilation in the Intra-Americas Sea with the Regional Ocean Modeling System (ROMS). *Ocean Modelling*, *23*, 130–145. https://doi.org/10.1016/j.ocemod.2008.04.008

Shchepetkin, A. F., & McWilliams, J. C. (2005). The Regional Ocean Modeling System: A split-explicit, free-surface, topography following coordinates ocean model. *Ocean Modelling*, *9*, 347–404. https://doi.org/10.1016/j.ocemod.2004.08.002

Sheng, J., Tang, L., & Ji, X. (2010). An examination of seasonal mean circulation and salinity distributions in the Pearl River Estuary of China using a triply-nested coastal ocean circulation model. *Proceedings of 11th Estuarine and Coastal Modeling*, 108–127.

Shu, Y., Zhu, J., Wang, D., Yan, C., & Xiao, X. (2009). Performance of four sea surface temperature assimilation schemes in the South China Sea. *Continental Shelf Research*, *29*, 1489–1501. https://doi.org/10.1016/j.csr.2009.03.016

Song, Y. T., & Haidvogel, D. B. (1994). A semi-implicit ocean circulation model using a generalized topography following coordinate system. *Journal of Computational Physics*, *115*, 228–244. https://doi.org/10.1006/jcph.1994.1189

Stammer, D., Wunsch, C., Giering, R., Eckert, C., Heimbach, P., Marotzke, J., et al. (2002). Global ocean circulation during 1992–1997, estimated from ocean observations and a general circulation model. *Journal of Geophysical Research: Oceans*, *107*, 3118. https://doi.org/10.1029/2001JC000888

Teruzzi, A., Bolzon, G., Salon, S., Lazzari, P., Solidoro, C., & Cossarini, G. (2018). Assimilation of coastal and open sea biogeochemical data to improve phytoplankton simulation in the Mediterranean Sea. *Ocean Modelling*, *132*, 46–60. https://doi.org/10.1016/j.ocemod.2018.09.007

Trodahl, M., & Lsachsen, P. E. (2018). Topographic Influence on Baroclinic Instability and the Mesoscale Eddy Field in the Northern North Atlantic Ocean and the Nordic Seas. *Journal of Physical Oceanography*, *48*, 2593–2607. https://doi.org/10.1175/jpo-d-17-0220.1

Xie, J. P., Counillon, F., Zhu, J., & Bertino, L. (2011). An eddy resolving tidal driven model of the South China Sea assimilating along-track SLA data using the EnOI. *Ocean Science*, *7*, 609–627. https://doi.org/10.5194/os-7-609-2011

Xie, J. P., & Zhu, J. (2010). Ensemble optimal interpolation schemes for assimilating Argo profiles into a hybrid coordinate ocean model. *Ocean Modelling*, *33*, 283–298. https://doi.org/10.1016/j.ocemod.2010.03.002

Zhang, W. G., Wilkin, J. L., & Arango, H. G. (2010). Towards building an integrated observation and modeling system in the New York Bight using variational methods. Part I: 4DVAR data assimilation. *Ocean Modelling*, *35*, 119–133. https://doi.org/10.1016/j.ocemod.2010.08.003

Zu, T., & Gan, J. (2009). Process-oriented study of the circulation and river plume in the Pearl River Estuary: Response to the wind and tidal forcing. *Advances in Geosciences: Ocean Science*, *12*, 213–230. https://doi.org/10.1142/9789812836168_0015

Zu, T., & Gan, J. (2015). A numerical study of coupled estuary-shelf circulation around the Pearl River Estuary during summer: Responses to variable winds, tides and river discharge. *Deep Sea Research Part II*, *117*, 53–64. https://doi.org/10.1016/j.dsr2.2013.12.010

Zu, T., Gan, J., & Erofeeva, S. Y. (2008). Numerical study of the tide and tidal dynamics in the South China Sea. *Deep Sea Research Part I*, *55*, 137–154. https://doi.org/10.1016/j.dsr.2007.10.007